Surface Deformation and Seismic Rebound: Implications and Applications

Chieh-Hung Chen · Ta-Kang Yeh · Jann-Yenq Liu · Chung-Ho Wang · Strong Wen · Horng-Yuan Yen · Shu-Hao Chang

Abstract An earthquake process includes pre-seismic stress accumulation, co-seismic rock rupture and post-seismic elastic and/or viscoelastic rebound. Although co-seismic and post-seismic deformations have been readily observed using the global positioning system (GPS), detecting pre-seismic stress accumulation hidden in time-series data remains challenging. This study applies the Hilbert–Huang transform to extract non-linear and non-stationary pre-earthquake deformation data from GPS records for central Taiwan. By converting the derived surface deformation into horizontal azimuths, the randomly oriented GPS-azimuths are reoriented in a similar direction several days before and after earthquakes due to loading and rebound stress, respectively. Analytical results demonstrate that the stress accumulation and release along the entire course of an earthquake process provide significant evidence supporting the seismic rebound theory. This finding would be applicable to areas with dense GPS networks and active plate interactions. Surface deformations detected by the proposed analytical technique have encouraging potential for mitigating future seismic hazards.

C.-H. Chen · C.-H. Wang · S.-H. Chang
Institute of Earth Sciences, Academia Sinica, Taipei 115, Taiwan

T.-K. Yeh (✉)
Institute of Geomatics and Disaster Prevention Technology, Ching Yun University,
Jhongli 320, Taiwan
e-mail: bigsteel@cyu.edu.tw

J.-Y. Liu
Institute of Space Science, National Central University, Jhongli 320, Taiwan

J.-Y. Liu
Center for Space and Remote Sensing Research, National Central University, Jhongli 320, Taiwan

S. Wen
Institute of Seismology, National Chung Cheng University, Chiayi 621, Taiwan

H.-Y. Yen
Institute of Geophysics, National Central University, Jhongli 320, Taiwan

1 Introduction

Earthquakes result from abrupt tectonic movements between plates that are under enormous
stress. If loading stress on strata is less than the maximum static friction force, it would be
stored via rock deformation based on classical mechanisms (Den Hartog 1961; Ruina and
Pratap 2002). Once the sequential loading stress exceeds the threshold, which rocks can
withstand via deformation, weak sections of rock strata would experience sudden movements
and potentially give rise to earthquakes. Reid (1910) develops the elastic rebound theory
based on surface deformation in the 1906 San Francisco earthquake. The theory proposes that
elastic rocks are capable of stress accumulation. When the accumulated energy is partially (or
as completely as possible) released, dislocation happens in weak sites of strata during
earthquakes. On the other hand, previous studies have suggested that post-seismic rebounds
are closely related to viscoelastic behavior (Cohen 1994; Ueda et al. 2001; Wang 2007),
which can reasonably explain the rebound duration from a few days to even a few years as a
result of heat release during an earthquake and/or inhomogeneous materials in the crust.
Consequently, earthquakes can be explained by the following processes: stress is first stored
in deformed strata, second, rocks rupture at weak locations, and finally a sudden release of
accumulated stress occurs (Wang 2007), regardless of the rebound from elastic or viscoelastic
processes. However, both elastic and viscoelastic theories are partially supported by after-slip
observations during an earthquake. Loading stress on strata stored by deformation has not
been definitively proven by the elastic and viscoelastic theory.

Measurements of plate movements in terms of temporal and spatial deformation are very
important in the study of tectonic loading (Yu et al. 1997). Instruments taking advantage of
the global positioning system (GPS) capture emitted signals from orbiting satellites to
determine accurate locations on the Earth's surface (Prawirodirdjo and Bock 2004; Xu 2007).
Linear trends of long-term GPS records at regional scale are commonly used to develop the
world-wide plate movements (Yu et al. 1997; Wernicke et al. 2004; Mahmoud et al. 2005).
Since most conspicuous ruptures typically occur along a fault (the weakest section in rock
strata) within a very short time window and present the most common source of tectonic
earthquakes (Aki and Richards 2002), GPS measurements located either nearby or far away
from fault rupture zones are utilized to explain surface deformation associated with major
earthquakes (Yu et al. 2001, 2003; Gahalaut et al. 2006). Furthermore, the abrupt and intense
changes are generally related to co-seismic and post-seismic deformation (Yu et al. 2001,
2003; Gahalaut et al. 2006; Hsu et al. 2006, 2007). In addition, surface deformation involved
an extremely complex elastic behavior following the earthquakes. Thus, continuous GPS
observations for short temporal periods are valuable for characterizing the seismogenic
process and identifying the seismic source (Norabuena et al. 2004; Wang 2007). In this study,
pre-seismic and post-seismic deformations in a recent case of Taiwan (Fig. 1a) are examined
in detail to test and validate the rebound theory using GPS data.

2 Methodology

This study utilizes Bernese 5.0 software (Dach et al. 2007) to independently analyze the
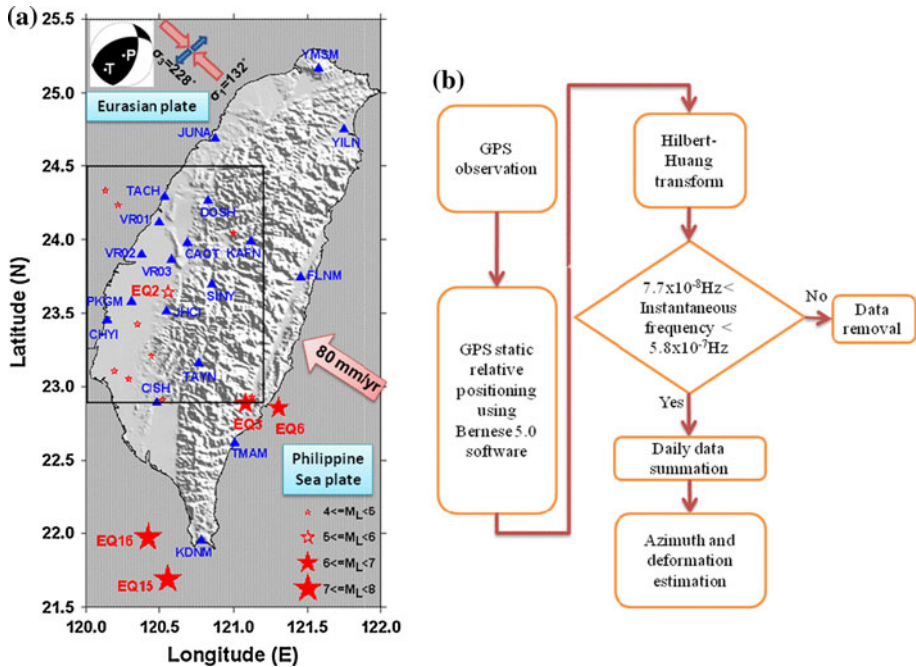double-differenced data phase (Fig. 1b). The tropospheric delay is corrected by the

Fig. 1 **a** Location map of Taiwan shows the studied earthquake epicenters (*open* and *solid red stars*) and GPS stations (*blue triangles*) in this work. EQ2 (*open red star*; M_L = 5.1, 2006/03/09), which is the largest earthquake in the study area (*solid square*) in 2006, is utilized to understand changes of the GPS-azimuths during earthquakes. The study area as shown in the solid square covers a range of 22.9–24.5°N, 120.0–121.2°E. The associated fault plane solutions with the P (most compressive) and T (least compressive) axes are presented in the *upper left* plot. By its side, a diagram illustrates σ_1 and σ_3 that are responsible for the *P* and *T* axes. **b** The flow chart for the data analysis process in this study. GPS variations at the N–S, E–W and vertical components are computed by Bernese 5.0 software. Two horizontal components are filtered by the band-pass filter (20–150 days) using HHT to evaluate the daily surface deformations and the GPS-azimuths

Saastamoinen model (Saastamoinen 1973) with an elevation-dependent weighting of $\cos^2(z)$, where z is the zenith distance. Wet tropospheric correction is applied at hourly intervals for estimating the Zenith Troposphere Delay of GPS signals (Wang et al. 2008). Moreover, ionospheric delay and satellite clock errors are eliminated by using a combination of GPS data at L1 and L2 frequencies and the International GNSS Service (IGS) sp3 precise ephemerides, respectively (Yeh et al. 2009).

When signals, which are emitted from satellites and recorded by GPS instruments on the Earth's surface, are computed by the above processes, the obtained GPS data accurately describe horizontal movements near the stations. Long-term variations in displacement over the study period can be determined using continuously recording instruments. Notably, GPS data over a long period may contain long-term crustal deformation caused by continent/plate drift (Ruina and Pratap 2002), and annual/semiannual effects resulting from tropospheric delay, ionospheric refraction and ocean tidal loading (Van Dam et al. 2001; Blewitt and Lavallee 2002; Ray et al. 2008; Yeh et al. 2008). Furthermore, discontinuous co-seismic displacements are hidden behind these long-term values despite sequential observation. Although the Fourier transform and the wavelet transform are commonly employed to process the linear and/or stationary signals, they are insufficient to extract

discontinuous, non-linear and non-stationary displacements such as GPS co-seismic displacements. In this work, GPS data are filtered using the Hilbert–Huang transform (HHT) (Huang et al. 1998, 2003; Huang and Wu 2008) to reduce noise and long-term effects (Van Dam et al. 2001; Blewitt and Lavallee 2002; Ray et al. 2008; Yeh et al. 2008).

HHT contains two steps; the empirical mode decomposition (EMD) and the Hilbert transform (Huang et al. 1998). GPS data in each component through EMD generate several intrinsic mode functions (IMFs) depending upon energy characteristics to achieve the Hilbert transform. In EMD, sifting plays an important role to exact IMFs (Huang et al. 1998); here, every point of analyzed data is subtracted by averages of envelopes, which are computed by local maxima and minima of analyzed data through a cubic spline method. This method replaces regular *sine* or *cosine* waves of the Fourier transform and basic functions of the wavelet transform to better adapt discontinuous, non-linear and non-stationary nature of signals (for more details see Huang et al. 1998). For example, EMD is utilized to decompose the first IMF from one component of GPS data. Difference is derived by subtracting the means of envelopes from the initial GPS data (i.e. sifting). IMF can be determined if the mean of the difference is smaller than 10^{-6} m in this study. Moreover, the difference would replace the initial GPS data to repeat sifting if their mean is greater than 10^{-6} m. Through the iterative sifting process, IMFs with similar energy characteristics can be effectively extracted. The resultant IMFs are further removed from the initial GPS data one by one and residuals as found in the initial GPS data are again used to repeat EMD. EMD is terminated once the associated envelopes cannot be generated due to insufficient numbers of local maxima and minima. Entire IMFs are subsequently transferred into the frequency domain using the Hilbert-transform, where the instantaneous frequency and amplitude at each point in every IMF can be obtained. Finally, points in each IMF not only present quantitative GPS displacements in the time domain, but also provide instantaneous frequency and amplitude in the frequency domain. Quantitative GPS displacements at instantaneous frequency within a band-pass filter of 20–150 days (7.7×10^{-8} to 5.8×10^{-7} Hz) recorded at the same time are superposed to generate a new time-series of GPS displacements. Meanwhile, the filtered GPS displacements in the northern-southern and eastern-western components are further employed to evaluate the GPS-azimuths and horizontal surface displacements closely associated with earthquakes (Fig. 1b).

3 Observations

Taiwan is located along the active western circum-Pacific seismic zone where the Philippine Sea plate moving North West at a rate of about 80 mm/year toward the Eurasian plate (Ho 1988; Liu et al. 2009). This region can be divided into the Central Range, Western Foothills and Coastal Range based on its geological characteristics (Ho 1988). The Coastal Range is composed of the Philippine Sea plate which exerts a persistent northwestern movement against the Eurasian plate. The intense collision between two plates yielded the principal Central Range with a maximum elevation up 3,952 m on a roughly North-South alignment. The Western Foothills are located at the western side of the principal Central Range, where the surface topography features plains and hills with a parallel alignment in the North-South direction. Our study area concentrates at a range of 22.9–24.5°N and 120.0–121.2°E in the Western Foothills due to a dense coverage of GPS stations and relative long time-gap in earthquake series (Fig. 1a).

Plate collision has generated numerous earthquakes in Taiwan (Tsai 1986). To better monitor these earthquakes, the broadband array for seismology (BATS) in Taiwan has routinely recorded earthquake events since 1996 (http://tecdc.earth.sinica.edu.tw/TEC/db/) (Kao et al. 2002; Liang et al. 2003, 2004). In 2006, 12 earthquakes with $M_L \geq 4.0$ occurred in the study area (Table 1). The largest, EQ2 (2006/3/9, $M_L = 5.1$; 23.64°N, 120.56°E), with a shallow depth of 9.9 km is used as the main target in this study (the red star in Fig. 1a). To further understand primary azimuths of stress loading, the observed polarities of seismic P-waves are utilized to invert the orientation of principal stress axes by adopting the method proposed by Robinson and McGinty (2000). The principal axes, σ_1 (most compressive) and σ_3 (least compressive), are derived from this method and also can be expressed as the P and T axes, respectively. For EQ2, the azimuths and dips of the P axis are (132.78°, 3.41°) and those of the T axis are (228.96°, 60.55°). Earthquakes with a large magnitude ($M_L \geq 6.0$), which impacted large areas, are also taken into account, though they are outside the study area (EQs 3, 6, 15 and 16 in Table 1). Thirteen GPS stations within the study area are selected for detailed examinations, and the other 6 outside the study range but with long observation periods are also used for reference (Table 2). These GPS stations exhibit high resolution with a 30-seconds sampling interval. GPS data are calculated by a relative static positioning between Kinmen (KMNM) (24.46°N, 118.39°E) with these 19 stations during the entire study period. The continuous recording KMNM station is located in South East mainland China on the Eurasian plate, and has distances of about 210–340 km away from the GPS array in Taiwan. The coordinates of the KMNM station were precisely determined using the International Terrestrial Reference Frame 2000 (ITRF2000) for geocentric coordinates and the 1980 Geodetic Reference System (GRS80) for the reference ellipsoid.

Table 1 The earthquake catalog in 2006 for $M_L \geq 4$ in the study area and for $M_L \geq 6$ in Taiwan region

ID	Year	Month	Day	Hour	Minute	Second	Lat. (°N)	Long. (°E)	Depth (km)	M_L
EQ1	2006	2	23	20	19	5.94	24.0446	120.997	24.98	4.6
EQ2	2006	3	9	4	7	28.79	23.6445	120.5581	9.93	5.1
EQ3	2006	4	1	10	2	19.54	22.8835	121.0806	7.2	6.2
EQ4	2006	4	4	6	48	32.05	22.9265	121.121	7.29	4.5
EQ5	2006	4	5	3	35	33.3	22.9286	121.1243	7.23	4
EQ6	2006	4	15	22	40	55.37	22.8555	121.3035	17.9	6
EQ7	2006	4	18	1	26	1.06	23.4208	120.3448	10.62	4.6
EQ8	2006	5	24	20	52	41.33	22.9	121.077	7.76	4.3
EQ9	2006	6	4	1	27	30.75	23.0505	120.2853	14.58	4.1
EQ10	2006	6	11	8	57	52.33	23.2061	120.4423	9.52	4.2
EQ11	2006	6	17	2	4	47.89	23.104	120.1893	15.93	4.3
EQ12	2006	7	30	15	37	8.22	24.3336	120.1275	26.19	4.1
EQ13	2006	8	12	18	15	36.42	22.9068	120.5191	15.97	4.2
EQ14	2006	11	6	18	39	36.32	24.2348	120.2146	25.01	4.2
EQ15	2006	12	26	12	26	21	21.6873	120.5553	44.11	7
EQ16	2006	12	26	12	34	15.13	21.9698	120.4196	50.22	7

Table 2 Coordinates of the GPS stations in this study

Station Name	Latitude	Longitude	Height (m)
CAOT	23°58′45.7953″	120°41′19.4489″	141.6913
CHYI	23°27′2.7766″	120°8′24.5577″	22.9962
CISH	22°53′22.5415″	120°28′52.4255″	90.8568
DOSH	24°15′45.6804″	120°49′36.7613″	396.2881
FLNM	23°44′46.7074″	121°27′12.0718″	138.5026
JHCI	23°30′49.4287″	120°32′50.7053″	150.9317
JUNA	24°41′2.2345″	120°52′31.3275″	45.3942
KAFN	23°59′15.3242″	121°6′59.3571″	1584.813
KDNM	21°56′57.9339″	120°46′55.2714″	58.2746
PKGM	23°34′47.6206″	120°18′19.7968″	42.8094
SINY	23°41′47.3837″	120°51′11.5329″	536.3169
TACH	24°17′27.0365″	120°32′6.4691″	33.8158
TAYN	23°9′33.6516″	120°45′51.1080″	645.6569
TMAM	22°36′57.8957″	121°0′26.9268″	58.7401
VR01	24°7′1.8072″	120°29′53.6541″	39.405
VR02	23°53′59.7882″	120°22′24.5331″	42.8023
VR03	23°51′51.9580″	120°34′53.4448″	77.3492
YILN	24°44′45.8919″	121°44′44.3441″	64.0505
YMSM	25°9′56.5736″	121°34′26.5952″	784.0468

4 Results

First, the northern-southern component of GPS data at the PKGM station (Table 2) in 2006 (Fig. 2a) is taken as an example to illustrate the band-pass filtering results using HHT. The GPS data can be decomposed into 9 IMFs (Fig. 2b–j) and a residual (Fig. 2k) by using EMD. To comprehend characteristics of these IMFs, we compute the median of each IMF by using their instantaneous frequencies (Table 3). $IMF_{1–5}$ with the similar medians between 7.288×10^{-7} Hz (period = 15.9 days) and 1.439×10^{-6} Hz (period = 8.04 days) are considered to be noise. The medians from IMF_6 to IMF_9 are gradually graded down to 9.191×10^{-8} Hz (period = 125.9 days) that approaches semiannual signals. Therefore, an effective band-pass filter is needed to differentiate noise and long-term effects.

Figure 3a shows noise superimposed by points of IMFs at the instantaneous frequency $>5.787 \times 10^{-7}$ Hz (period = 20 days). Surprisingly, variations for filtered noise (Fig. 3a) have relatively large fluctuations during 160–255 days in summer of 2006. The filtered noise agrees with previous studies that the GPS displacements generally have large fluctuations in the summer due to disturbances in the atmosphere and ionosphere (Van Dam et al. 2001; Blewitt and Lavallee 2002; Ray et al. 2008; Yeh et al. 2008). Figure 3b shows reduced fluctuations after noise is subtracted from the GPS data. Notably, long-term crustal deformation, annual variations and semiannual effects still remain. To understand long-term effects, we superimpose points of IMFs at the instantaneous frequency $<7.716 \times 10^{-8}$ Hz (period = 150 days) and add them to the residual (Fig. 3c). Once the noise (Fig. 3a) and the long-term effects (Fig. 3c) are both subtracted, the GPS data have
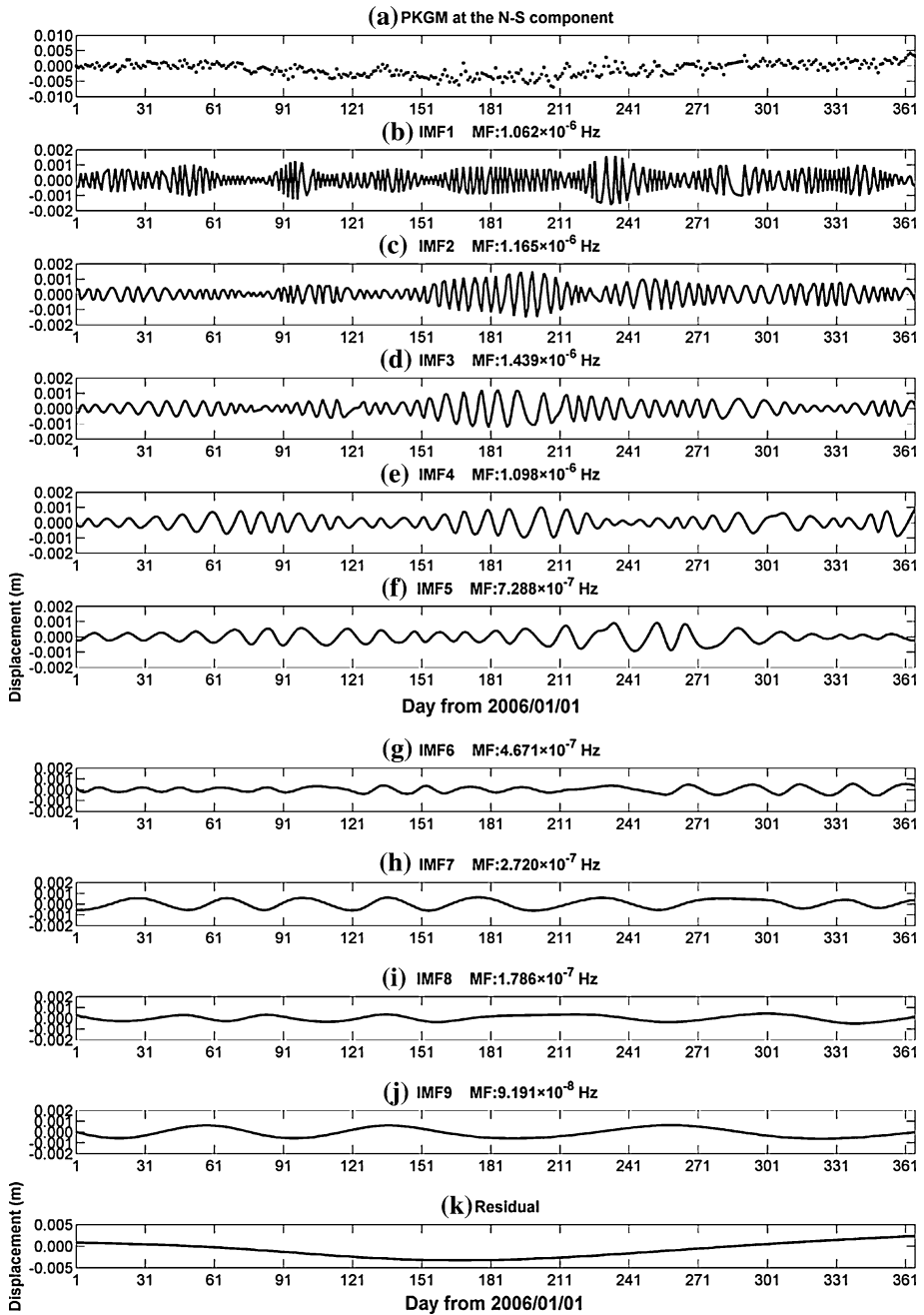
Fig. 2 The GPS displacement at the N–S component in the PKGM station and its IMFs in 2006. The frequency following IMF denotes the median instantaneous frequency of each IMF mode

Table 3 The median frequency and period of each IMF derived by the GPS data at the northern-southern component in the PKGM station

IMF	Median frequency (Hz)	Median period (day)
1	1.062×10^{-6}	10.9
2	1.165×10^{-6}	9.94
3	1.439×10^{-6}	8.04
4	1.098×10^{-6}	10.5
5	7.288×10^{-7}	15.9
6	4.671×10^{-7}	24.8
7	2.720×10^{-7}	42.5
8	1.786×10^{-7}	64.8
9	9.191×10^{-8}	125.9
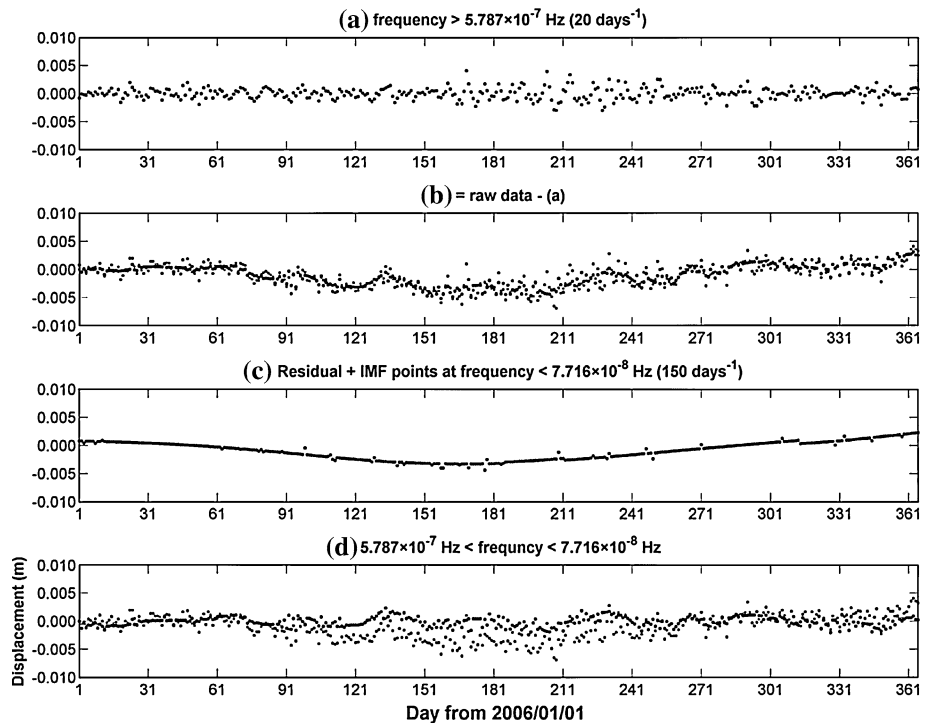
Fig. 3 Variations of the GPS displacement at the N–S component filtered by distinct frequency bands in the PKGM station. The points of IMFs filtered by the distinct frequency bands of $>5.787 \times 10^{-7}$ Hz at the same observation time are superimposed as noise and are presented in (**a**). *Black solid circles* in (**b**) denote remains given by subtracting noise from input data. Note that the *shadow solid circles* present input data for comparison. Input data filtered with a frequency band of $<7.716 \times 10^{-8}$ Hz are combined with the residual as long-term effects shown in (**c**). We subtract the noise, long-term effects and residual generated by HHT from input data to yield deformation associated with earthquakes displayed in (**d**). Similarly, the *shadow solid circles* denote input data for comparison

been filtered by using a band-pass filter of 7.716×10^{-8} to 5.787×10^{-7} Hz. The filtered GPS displacement at the northern-southern component is relative to that of the eastern-western component to yield the GPS-azimuths and horizontal surface displacements.

Figure 4 illustrates the time-sliced deformations before and after EQ2 in the study area. Figure 4a and f show that the GPS-azimuths of a certain period are normally disorganized and arbitrarily oriented after the long-term deformation has been removed through the data process. However, the observed GPS-azimuths among the GPS stations appear to align a few days before EQ2 due to stress loading (Fig. 4b). The majority of deformations exceeded 1 mm in the study area. As EQ2 approaches, sharp decrease deformations suggest that stress is transferred into elastic energy stored via rock deformations (Fig. 4c). These deformations then disrupt the alignment of the GPS-azimuths on the surface. For a large thrust earthquake with an apparent surface rupture, upward and downward displacements in the vertical component can be measured in the hanging and foot walls, respectively. Displacements in the horizontal component direct toward a thrust fault. Regarding EQ2 with a magnitude (M_L) of 5.1 in this study, the associated fault length is about 2–5 km. EQ2 occurred without surface rupture due to its depth down to about 9.9 km. It is difficult to observe the co-seismic deformation associated with EQ2. In contrast, the filtered GPS data show small deformation near the epicenter of EQ2 (Fig. 4d). The GPS-azimuths in Fig. 4d are still disordered and show similar patterns as those presented in Fig. 4c. After the main shock, the GPS-azimuths become parallel, but in the opposite directions (Fig. 4e). These features indicate that when stored elastic energy is released after EQ2, GPS deformation does provide concrete evidence for pre- and post-seismic deformations in accordance with the seismic rebound theory. Several days later, as the stress is unloaded from rocks, the GPS-azimuths become disorganized again (Fig. 4f).

We use diagrams (Fig. 5) to illustrate the direction of the GPS-azimuths of EQ2. Figure 5a shows the scattered distribution obtained from the GPS-azimuths covering the entire year of 2006. For the period of days 15–25 before EQ2 (Fig. 4a; days 43–53 after 1 January 2006), the GPS-azimuths are randomly distributed through 0–360° and no apparent directions can be discerned (Fig. 5b). During the period of 6–16 days before EQ2 (Fig. 4b; days 52–62 after 1 January 2006), the GPS-azimuths are confined to a range within 240–315° (Fig. 5c), which is generally toward the West and roughly perpendicular to the fault strike (18°). Note that σ_1 (i.e. the maximum horizontal compressive stress) at 132° and the range derived by the associated deformation show an agreement. This observation suggests that stress sequentially loads on rocks and/or strata, thus yielding surface deformation in the similar directions. On the very day of EQ2 (Fig. 4c; days 63–73 since 2006/1/1), the GPS-azimuths returned to random order without a particular orientation (Fig. 5d). The GPS-azimuths have changed to accommodate more loading stress when the latter approaches the threshold of rock strength. The azimuth distributions between 65 and 135° (Fig. 5e) on days 0–10 after EQ2 (days 68–78 since 2006/1/1) are opposite to those of Fig. 3c and perpendicular to the strike (18°). The distribution of stress appears random in the period of 15–25 days after EQ2 (days 83–93 since 2006/1/1), implying that stress is unloaded from strata (Fig. 5f). Thus, the filtered GPS measurements in terms of the surface azimuths can be used to validate the seismic rebounds during earthquakes.

5 Discussion and Conclusions

Post-seismic stress changes are generally referred to an after-slip on the fault plane or viscoelastic/elastic relaxations in the rebound duration ranging from a few days to years (i.e. the seismic cycle). The post-seismic deformations after the 1993 Hokkaido Nansei-oki and 1964 Niigata earthquakes are related to viscoelastic relaxation (Hu et al. 2004), but are not identified for other earthquakes (Miura et al. 1990). The GPS-azimuths in this study
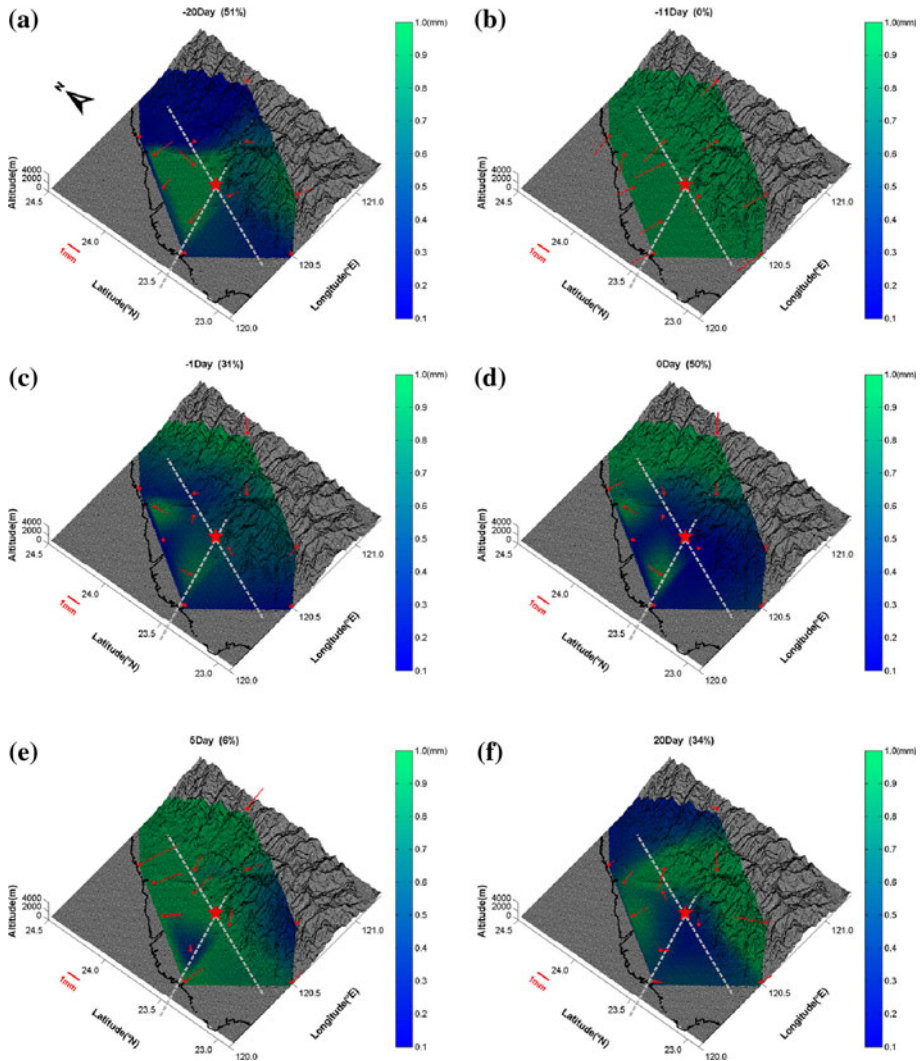
Fig. 4 Surface deformation at pre-, co- and post-seismic deformation stages. The *star* and *two dashed lines* denote the earthquake epicenter and strikes of the fault plane solutions, respectively. The *red lines* extended from the GPS stations (*red circles*) indicate the surface deformations and GPS-azimuths. The colored shades on the topography also show the intensity of daily surface deformations. For the pre-seismic deformation stage, GPS surface deformations on 20, 11 and 1 days before the sample earthquake (2006/03/09) are shown in **a**, **b** and **c**, respectively. The surface deformation and the GPS-azimuths on the very day of the earthquake are shown in (**d**). The post-seismic surface deformations at 5 and 20 days after the earthquake are shown as **e** and **f**, respectively. Note that the percentages following days to the earthquake indicate ratios of deformation <0.0005 m to the study area

suggest that displacements may be re-aligned into a similar orientation in response to the loading stress. The observations of the GPS-azimuth shifting before and after earthquakes can be used to differentiate the post-seismic stress changes with the after-slip on the fault plane or viscoelastic/elastic relaxations (Hsu et al. 2007). If the major GPS-azimuths remain unchanged before and after earthquakes, effects of pre-seismic stress loading last
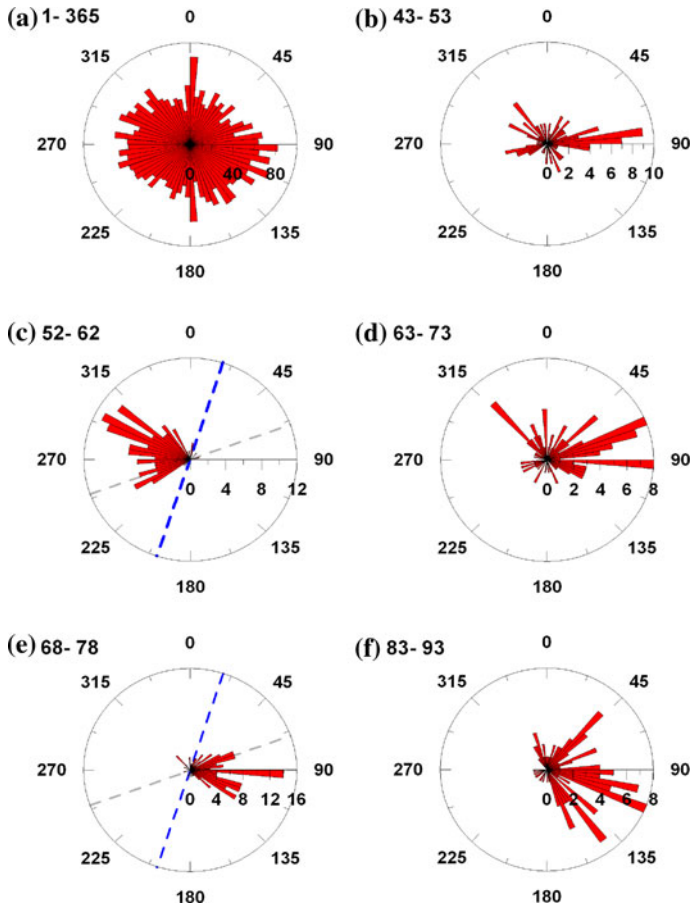
Fig. 5 *Rose* diagrams of the GPS-azimuths before and after the earthquake: **a** the reference rose diagram obtained by the GPS-azimuths for the entire year 2006; **b–f** are given by the GPS-azimuths between −5 and 5 days to the reference days in Fig. 4a, b, and d–f, respectively. The *blue* and *gray dashed lines* are the strikes of the fault and auxiliary fault planes as determined by the Geological Survey of Taiwan

for certain length of time. After-slip would be the dominant mechanism of post-seismic deformation in the short duration after a large earthquake. Conversely, when the reversed GPS-azimuths exist after an earthquake, viscoelastic/elastic relaxation of the lower crust and upper mantle would become relatively prominent as in this study. Thus, post-seismic deformation as evidenced in this study is an important and effective constraint for physical fault properties and the viscoelastic/elastic structure of a rock medium. The orientation of crustal deformation during earthquakes can be further utilized to examine and comprehend the proposition by Felzer et al. (2004) stating foreshocks, doublets, and aftershocks are simply different names for the same earthquake-triggering phenomena on different magnitude scales.

Although these phenomena are highly related to the seismic rebound theory, they might be caused by data evaluation between the selected reference-site (KMNM) with other observation stations. To clarify this possible artifact, a simple index (Fig. 6), which is given by an inverse of an average of the GPS-azimuth difference between every two
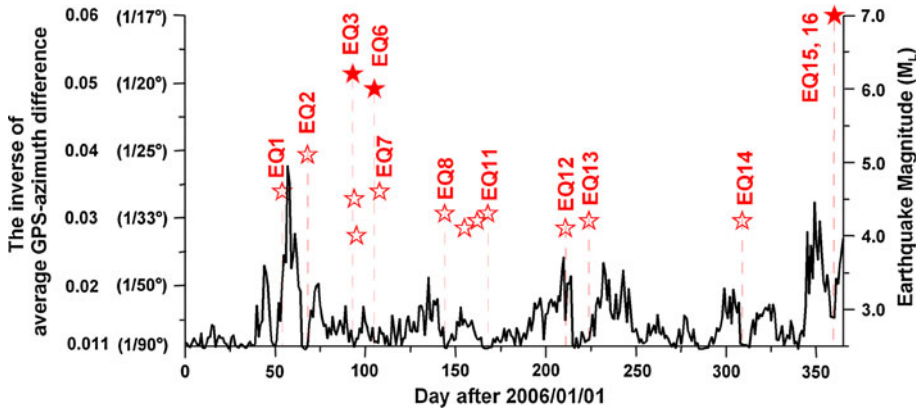
Fig. 6 The index associated with the GPS-azimuths in 2006. The index is an inverse given by the average difference of the GPS-azimuths between every two stations. The low (or high) index suggests that the GPS-azimuths have large (or small) difference to suggest that unsystematic (systematic) directions. The open ($M_L < 6$) and solid ($M_L \geq 6$) *red stars* and *vertical dashed lines* denote the earthquake occurrence dates

stations, is constructed and compared with the earthquakes listed in Table 1 ($M_L \geq 4$ for the study area and $M_L \geq 6$ for the Taiwan region). Here, a seismic cycle is used to illustrate changes of the index. When stress associated with earthquakes does not load on strata, the filtered deformations of GPS-azimuths at distinct stations show random orientations, particularly when responses from short-term noise and long-term crustal movements are removed (Figs. 4a, 5b). As the difference in the GPS-azimuths between two stations is increased, the inverse of the average difference (as the index) is decreased. In contrast, when stress associated with earthquakes loads on strata to produce parallel displacements at stations, the difference in the GPS-azimuths is reduced and produces a high index (see Figs. 4b, 5c). In reality, strata could not store unlimited stress. When loading stress exceeds a critical threshold in rocks, a rupture occurs and the GPS-azimuths become disordered resulting in a low index (Figs. 4c, d, 5d). According to the seismic rebound theory, pre-stored strain is released after earthquakes (Figs. 4e, 5e). The released force, which functions as loading stress, runs parallel to the GPS-azimuths yielding a high index. When the released force is spread over time, stress is unloaded and the disordered GPS-azimuths are observed with a low index (Figs. 4f, 5f).

Index variations for Taiwan earthquakes in 2006 are compared in detail (Fig. 6). The index generally remains at very low stages ($\sim$0.011 meaning that the average difference between the GPS-azimuths is about 90°) during a period with little seismic activity. The index increases suddenly to about 0.0377 (26.5° for the average difference) several days before EQ2 and agrees with the stressed GPS-azimuths moving toward a parallel orientation (Fig. 5b). The index then decreases sharply back to the low stage ($\sim$0.011) in the immediate days before EQ2 because stress has been sufficiently stored via rock stratum deformation. Since displacements are primarily caused by the seismic rebound, the index increases again up to 0.0203 (49.26° for the average difference) several days after EQ2 and is consistent with observation results (Fig. 5e). The index variations in response to stress loading and unloading during EQ2 are also observed in EQs 1, 3, 8, 11, 12, 13, 14, 15 and 16 in 2006 (Fig. 6, also see Appendix). Note that the observation in the study and the index variations associated with the 1999 Chi-Chi earthquake ($M = 7.6$, also shown in Appendix) yield an agreement. The indexes of the GPS-azimuths for the periods of high

seismicity during EQs 4–7 and EQs 9–10 are significantly lower due to a heavy distur-bance of stress overlap in a dense series of earthquakes.

Notably, the GPS-azimuths with the high index in the study area have a distance of ~100 km away from epicenters for strong EQs 15 and 16 ($M_L = 7$, see Appendix). Since fault rupture is considered the release of previously stored stress, the sum of loading stress causing pre-seismic deformation during seismogenic processes would be greater than the stress of an abrupt release from co-seismic displacements. Although areas of stress accumulation triggering earthquakes are not fully understood, they would be several times larger than fault rupture zones. Deformation in a seismogenic process and areas of stress accumulation are possibly underestimated when only rupture of associated faults is taken into account. Accordingly, the observation of EQs 15 and 16 indicates that (1) deforma-tions caused by stress accumulation are proportional to earthquake magnitudes, and (2) deformations can extend to areas beyond fault coverage for very large earthquakes. Thus, the observed deformations induced by stressed strata can be caused by both adjacent and large distant earthquakes. Seismogenic deformation associated with earthquakes is gen-erally studied by using two instruments located at a short spatial interval crossing fault rupture zones (Wyss et al. 1990). The debate regarding earthquake precursors in surface deformation (Wyss et al. 1990; Rogers and Dragert 2003) is possibly resulted from inhomogeneous structures within a local region. Since areas where stress accumulation triggers earthquake slips are quite large, all instruments located inside a study area can be utilized simultaneously to reduce failure risks and inconsistencies among precursors due to inhomogeneous structures.

Earthquake fault information is generally determined by fault plane solutions with aftershock distributions and/or geological surveys. However, as many earthquakes occur without surface ruptures, fault plane determination is extremely difficult. Based on observations of pre-, co- and post-seismic surface deformations using filtered GPS data, the orthogonal strike relative to the confined GPS-azimuths can provide auxiliary and useful information to determine a correct fault solution from the seismic rebound theory. The affected deformation confined to an apparent azimuth also indicates the stress influence extending further from a seismogenic stage. These surface deformation observations shed light on the timing and magnitude of an earthquake when the data processing can be automated in real-time mode and have the potential to mitigate future seismic hazards.

Appendix

In the main text, the target earthquake occurred on 68th day (March 9th) in 2006. Surface deformations on 48th, 57th, 67th, 68th, 73rd and 88th days are shown in Fig. 4 of the manuscript, respectively. The 5-days coverage graphs (both before and after) of GPS-azimuth distributions corresponding to plots of Fig. 4 are presented by Rose diagrams in Fig. 5. For a complete demonstration of the GPS-azimuth shifts during this earthquake, the slide file ('Appendix Figure.gif' that is a file at the following web-site at ftp://ftp.earth.sinica.edu.tw/pub/GPS%20Azimuths/) displays the surface deformation through a 40-days period before and after the main earthquake for reader's reference. In addition, three other cases were also supplied as supplementary (see below) to further support the GPS surface deformation induced by the seismic rebound phenomena.
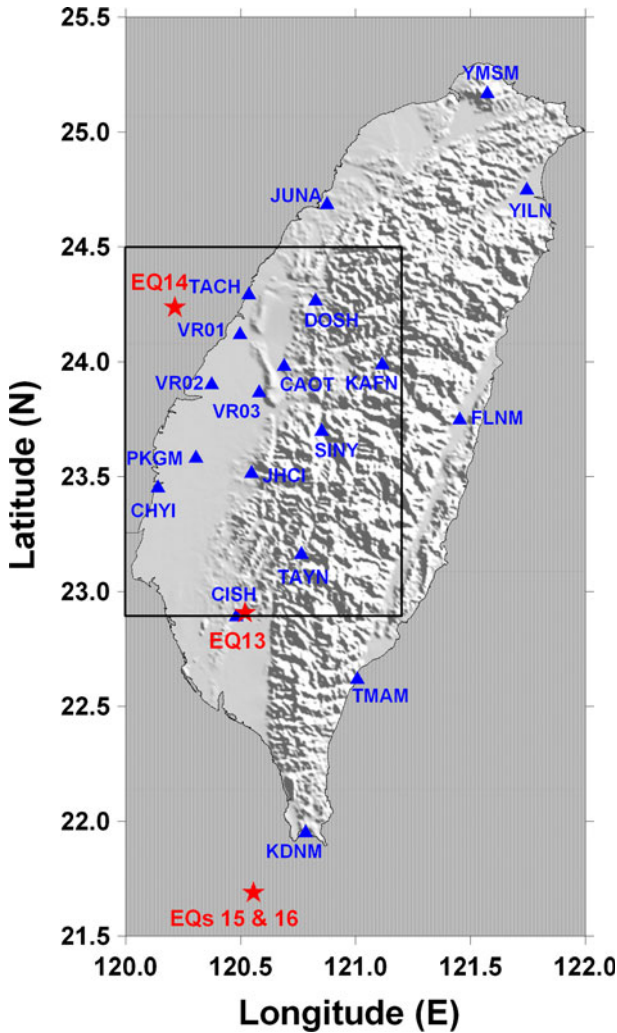
Fig. 7 Location map of three supplementary earthquakes (*red stars*) and GPS stations (*blue triangles*, same as the main text). Numbers following *EQ* indicate the occurrence day in 2006. EQ13 ($M_L = 4.2$) and EQ14 ($M_L = 4.2$) that located nearby or inside the study area (*rectangle range*) have relative small magnitudes. Although EQs 15 and 16 (double-let earthquakes) occurred in the far south to the study area (a distance of about 200 km), their relative large magnitude ($M_L = 7.0$) apparently affected the GPS surface deformation as well

The Case Study of the Chi-Chi Earthquake

Most GPS stations were mainly established after the Chi-Chi earthquake (20 September 1999, $M = 7.6$). Fifteen GPS stations (Fig. 14) are used here to compute the GPS index with available data. Figure 15 shows variations of the GPS index associated with the Chi-Chi earthquake using the same method of the manuscript. Similarly, the GPS-azimuths turned to parallel about 2–3 months before the Chi-Chi earthquake. The unclear rebound
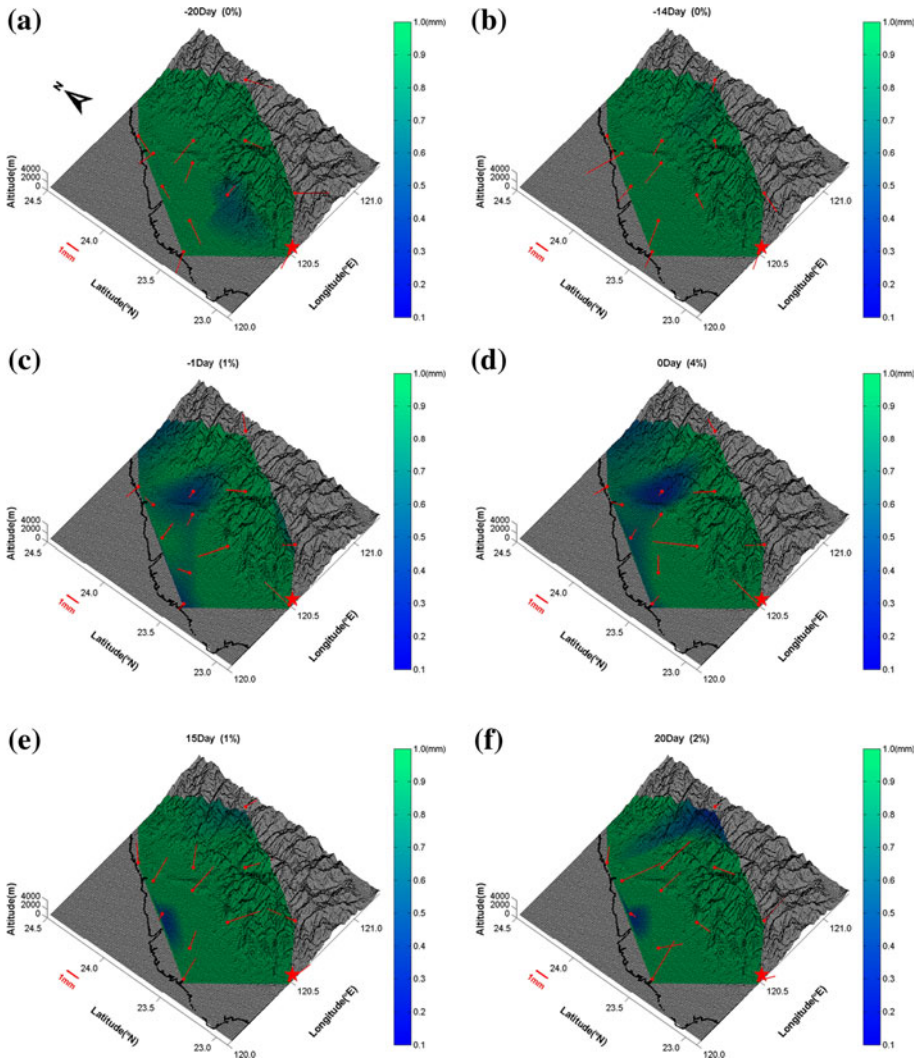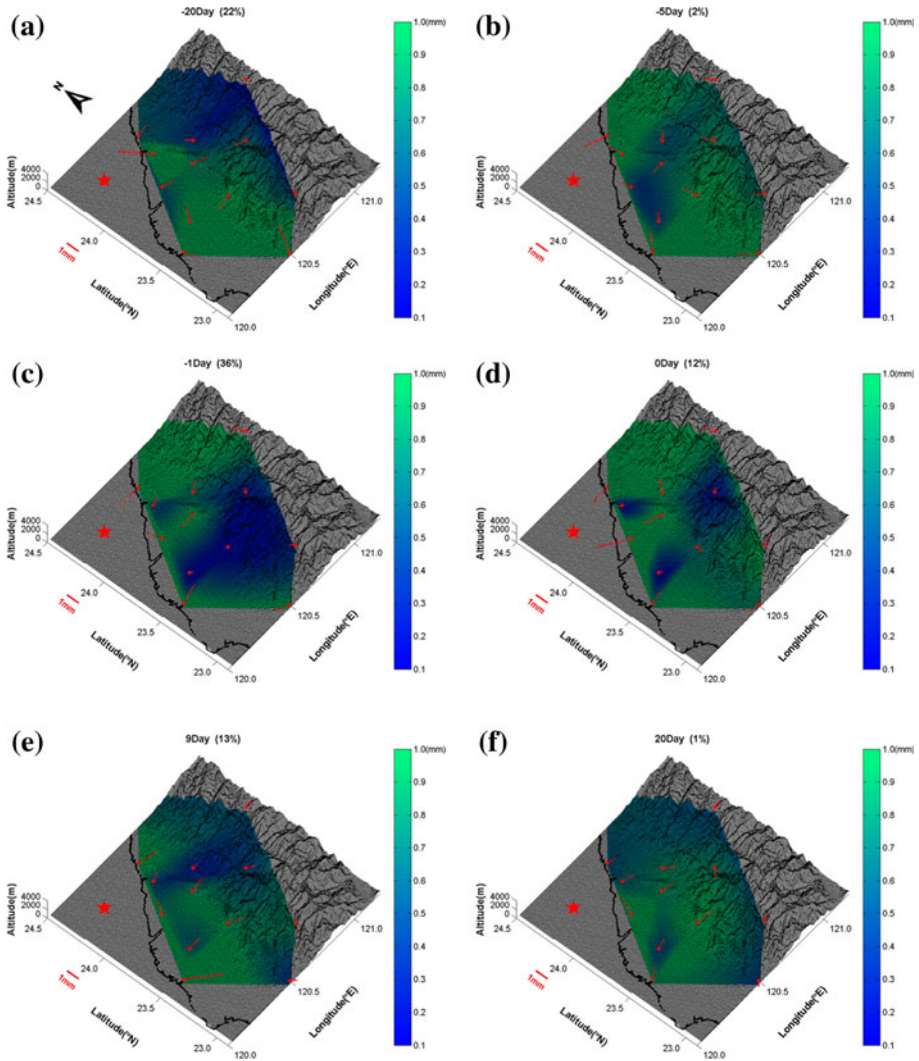
Fig. 8 GPS surface deformation associated with EQ13 (*red star*) in the study area. The surface azimuths of −20, −14, −1, 0, 15 and 20 days to EQ13 are shown from **a** to **f**, respectively. *Red lines* extended from the GPS stations (*red dots*) quantitatively exhibit azimuth deformations. *Color shades* on the topography indicate the relative intensity of the deformation. The numbers following each plot title represent the percentages with deformation <0.5 mm (i.e. insignificant portion as *blue colors*) relative to the total area

phenomena after the main shock are possibly affected by the following Chia-Yi earthquake (1999/10/22, $M = 6.4$) and/or accuracy damaged by intense surface deformation generated by the Chi-Chi earthquake.
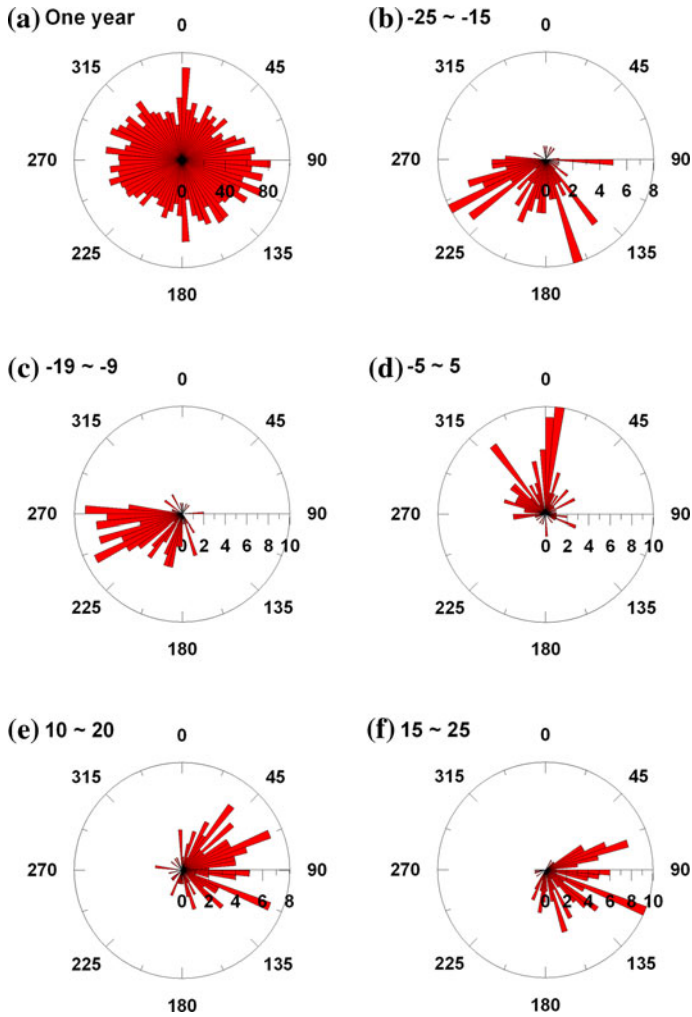
Fig. 9 The transformed GPS-azimuths associated with EQ13. *Rose diagrams* show the azimuth distributions during, **a** an entire year 2006 as base reference; and **b** −25 to −15 days; **c** −19 to −9 days; **d** −5 to 5 days; **e** 10–20 days; **f** 15–25 days to EQ13, and correspond to Fig. 8a, b, d, e, and f, respectively. In general, plots of **b**, **d**, and **f** show scattering patterns. By way of contrast, the distributions in **c** and **e** are confined in a smaller range, but in opposite directions
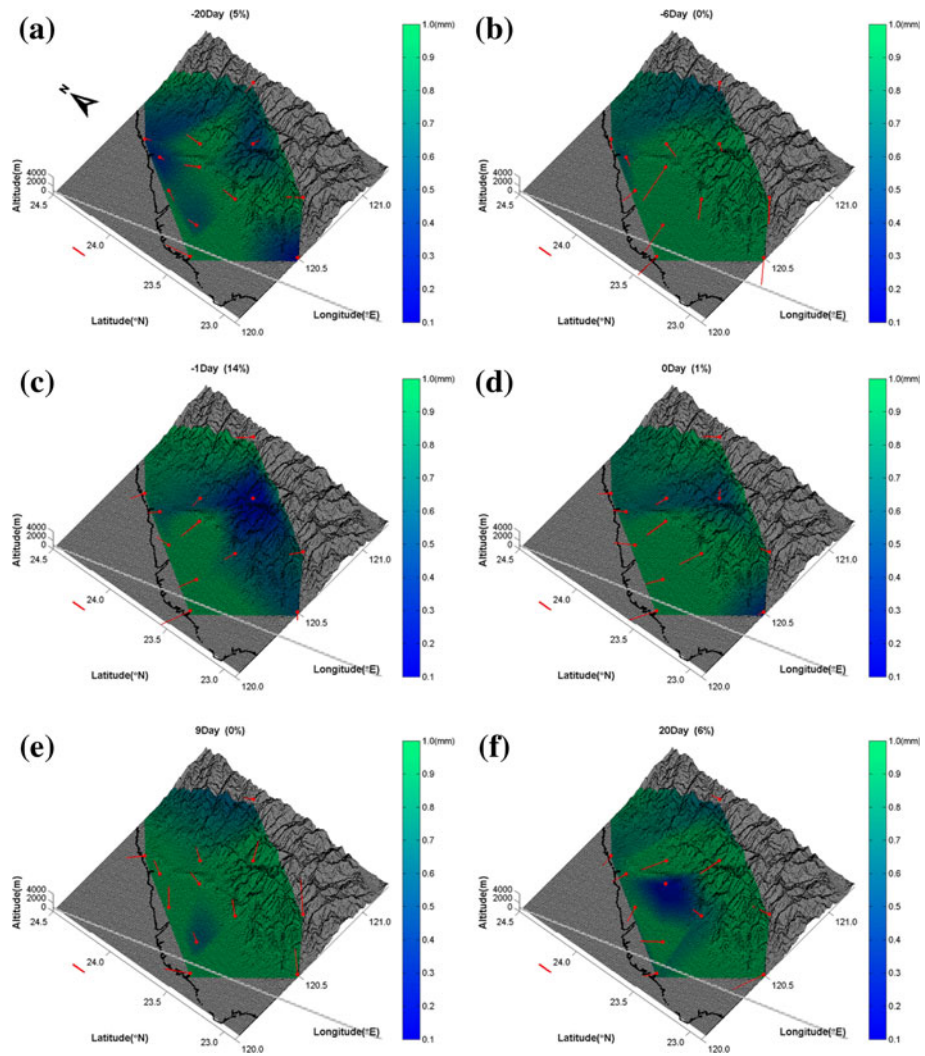
Fig. 10 GPS surface deformation associated with EQ14 (*red star*) in the study area. The surface azimuths of −20, −5, −1, 0, 9 and 20 days to EQ14 are shown from **a** to **f**, respectively. *Red lines* extended from the GPS stations (*red dots*) quantitatively exhibit azimuth deformations. *Color shades* on the topography indicate the relative intensity of the deformation. The numbers following each plot title represent the percentages with deformation <0.5 mm (i.e. insignificant portion as *blue colors*) relative to the total area
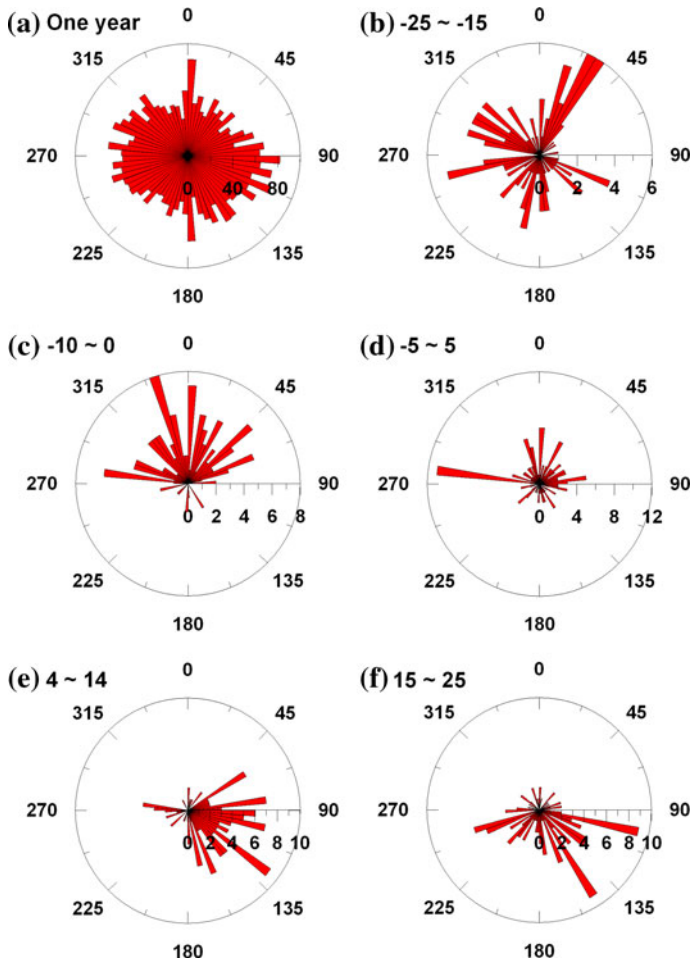
Fig. 11 The transformed GPS-azimuths associated with EQ14. *Rose diagrams* show the azimuth distributions during (**a**), an entire year 2006 as base reference; and **b**−25 to −15 days; **c** −10 to 0 days; **d** −5 to 5 days; **e** 4–14 days; **f** 15–25 days to EQ309, and correspond to Fig. 10a, b, d, e, and f, respectively. In general, plots of **b**, **d** and **f** show scattering patterns. By way of contrast, the distributions in **c** and **e** are confined in a smaller range, but in opposite directions

Fig. 12 GPS surface deformation associated with EQs 15 and 16 in the study area. The surface azimuths of −20, −6, −1, 0, 9 and 20 days to EQs 15 and 16 are shown from **a** to **f**, respectively. *Red lines* extended from the GPS stations (*red dots*) quantitatively exhibit azimuth deformations. *Color shades* on the topography indicate the relative intensity of the deformation. The numbers following each plot title represent the percentages with deformation < 0.5 mm (i.e. insignificant portion as *blue colors*) relative to the total area
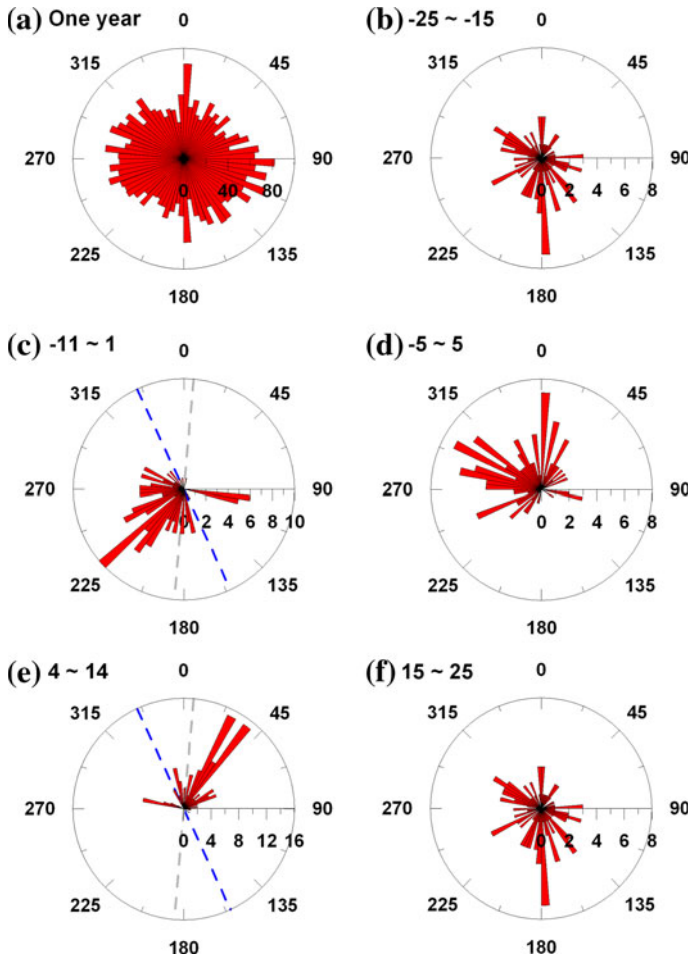
Fig. 13 The transformed GPS-azimuths associated with EQs 15 and 16. *Rose diagrams* show the azimuth distributions during (**a**), an entire year 2006 as base reference; and **b** −25 to −15 days; **c** −11 to 1 days; **d** −5 to 5 days; **e** 4–14 days; **f** 15–25 days to EQs 15 and 16, and correspond to Fig. 12a, b, d, e, and f, respectively. In general, plots of **b**, **d** and **f** show scattering patterns. By way of contrast, the distributions in **c** and **e** are confined in a smaller range, but in opposite directions. *Gray* and *blue dash lines* denote the strikes of the fault plane and auxiliary plane (Yen et al. 2008), respectively. Distributions in **c** and **e** are roughly orthogonal to the *blue dash line*, suggesting the *blue dash line* can be considered as the fault plane based on the seismic rebound theory. This observation agrees with the determination of Yen et al. (2008)
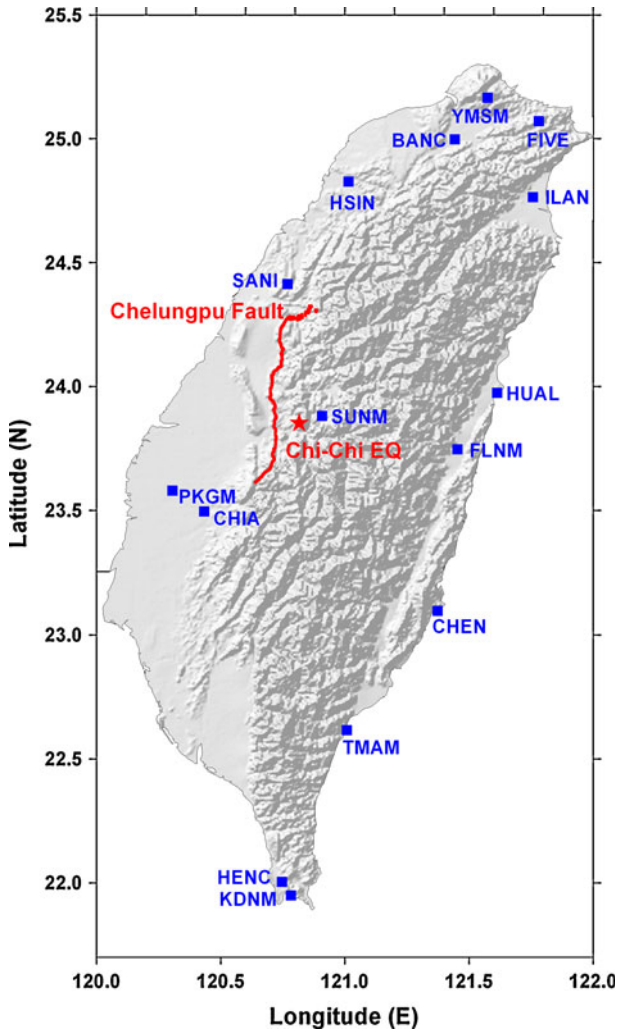
Fig. 14 Locations among the GPS stations, the Chelungpu fault and the epicenter of the Chi-Chi earthquake. *Blue squares* show the GPS stations with avaiable data. The *red line* and *star* denote the Chelungpu fault and the epicenter, respectviely
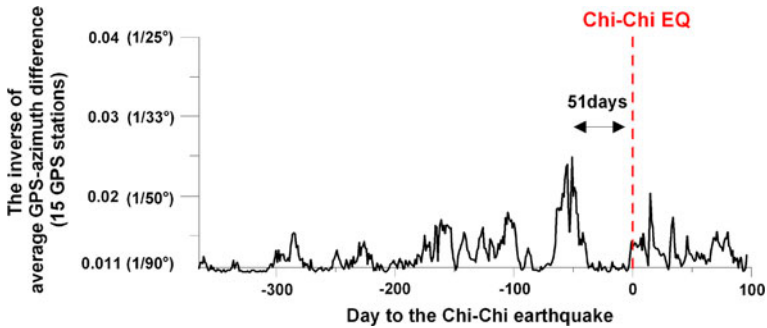
Fig. 15 The index associated with the GPS-azimuths during the Chi-Chi earthquake. The index is an inverse given by the average difference of the GPS-azimuths between every two stations. The low (or high) index suggests that the GPS-azimuths have large (or small) difference to suggest that unsystematic (systematic) directions

References

Aki K, Richards PG (2002) Quantitative seismology, 2nd edn. University Science Books, Sausalito

Blewitt G, Lavallee D (2002) Effect of annual signals on geodetic velocity. J Geophys Res 107(B7):2145. doi:10.1029/2001JB000570

Cohen SC (1994) Evaluation of the importance of model features for cyclic deformation due to dip-slip faulting. Geophys J Int 119:831–841

Dach R, Hugentobler U, Fridez P, Meindl M (2007) Bernese GPS software version 5.0. Astronomical Institute. University of Bern, Bern

Den Hartog JP (1961) Mechanics. Courier Dover Publications, New York

Felzer KR, Abercrombie RE, Ekström G (2004) A common origin for aftershocks, foreshocks, and multiplets. Bull Seism Soc Am 94:88–99

Gahalaut VK, Nagarajan B, Catherine JK, Skumar S (2006) Constraints on 2004 Sumatra Andaman earthquake rupture from GPS measurements in Andaman-Nicobar Islands. Earth Planet Sc Lett 242:365–374

Ho CS (1988) An introduction to the geology of Taiwan, 2nd edn. Central Geological Survey, The Ministry of Economic Affairs, Taipei

Hsu YJ, Simons M, Avouac JP, Galetzka J, Sieh K, Chlieh M, Natawidjaja D, Prawirodirdjo L, Bock Y (2006) Frictional afterslip following the Mw 8.7, 2005 Nias-Simeulue earthquake, Sumatra. Science 312:1921–1926

Hsu YJ, Segall P, Yu SB, Kuo LC, Williams CA (2007) Temporal and spatial variations of post-seismic deformation following the 1999 Chi-Chi, Taiwan earthquake. Geophys J Int 169:367–379

Hu Y, Wang K, He J, Klotz J, Khazaradze G (2004) Three-dimensional viscoelastic finite element model for postseismic deformation of the great 1960 Chile earthquake. J Geophys Res 109:B12403. doi:10.1029/2004JB003163

Huang NE, Wu Z (2008) A review on Hilbert–Huang transform: method and its applications to geophysical studies. Rev Geophys 46:RG2006

Huang NE, Shen Z, Long SR, Wu MC, Shih HH, Zheng Q, Yen NC, Tung CC, Liu HH (1998) The empirical mode decomposition and the Hilbert spectrum for nonlinear and non-stationary time series analysis. Proc R Soc Lond Ser A 454:903–995

Huang NE, Shen Z, Long SR, Shen SSP, Hsu NH, Xiong D, Qu W, Gloersen P (2003) On the establishment of a confidence limit for the empirical mode decomposition and Hilbert spectral analysis. Proc R Soc Lond Ser A 459:2317–2345

Kao H, Liu YH, Liang WT, Chen WP (2002) Source parameters of regional earthquake in Taiwan: 1999–2000 including the Chi-Chi earthquake sequence. Terr Atmo Ocean Sci 13:279–298

Liang WT, Liu YH, Kao H (2003) Source parameters of regional earthquake in Taiwan: January–December 2001. Terr Atmo Ocean Sci 14:249–260

Liang WT, Liu YH, Kao H (2004) Source parameters of regional earthquake in Taiwan: January–December 2002. Terr Atmo Ocean Sci 15:727–741

Liu CC, Linde AT, Sacks IS (2009) Slow earthquakes triggered by typhoons. Nature 459:833–836

Mahmoud S, Reilinger R, McClusky S, Vernant P, Tealeb A (2005) GPS evidence for northward motion of the Sinai Block Implications for E. Mediterranean tectonics. Earth Planet Sc Lett 238:217–224

Miura N, Sakai A, Taesiri Y, Yamanouchi K (1990) Polymer grid reinforced pavement on soft clay grounds. Geotext Geomembr 9:99–123

Norabuena E, Dixon TH, Schwartz S, DeShon H, Newman A, Protti M, Gonzalez V, Dorman L, Flueh ER, Lundgren P, Pollitz F, Sampson D (2004) Geodetic and seismic constraints on some seismogenic zone processes in Costa Rica. J Geophys Res 109:B11403. doi:10.1029/2003JB002931

Prawirodirdjo L, Bock Y (2004) Instantaneous global plate motion model from 12 years of continuous GPS observations. J Geophys Res 109:B08405. doi:10.1029/2003JB002944

Ray J, Altamimi Z, Collilieux X, Van Dam T (2008) Anomalous harmonics in the spectra of GPS position estimates. GPS Solut 12:55–64

Reid HF (1910) The mechanics of the earthquake, v. 2 of The California Earthquake of April 18, 1906: Report of the State Earthquake Investigation Commission: Carnegie Institution of Washington Publication 87 C192 p. 2

Robinson R, McGinty PJ (2000) The enigma of the Arthur's Pass, New Zealand, earthquake 2. The aftershock distribution and its relation to regional and induced stress field. J Geophys Res 105:16139–16150

Rogers G, Dragert H (2003) Episodic tremor and slip on the Cascadia subduction zone: the chatter of silent slip. Science 300:1942. doi:10.1126/science.1084783

Ruina A, Pratap R (2002) Introduction to statics and dynamics. Oxford University Press, Oxford

Saastamoinen J (1973) Contributions to the theory of atmospheric refraction. Bull Geod 107:13–34

Tsai YB (1986) Seismotectonics of Taiwan. Tectonophysics 125:17–38

Ueda H, Ohtake M, Sato H (2001) Afterslip on the plate interface following the 1978 Miyagi-Oki, Japan, earthquake, as revealed from geodetic measurement data. Tectonophysics 338:45–57

Van Dam T, Wahr J, Milly PCD, Shmakin AB, Blewitt G, Lavallee D, Larson KM (2001) Crustal displacements due to continental water loading. Geophys Res Lett 28:651–654

Wang K (2007) Elastic and viscoelastic models of crustal deformation in subduction earthquake cycles. In: Dixon TH, Moore JC (eds) The Seismogenic Zone of Subduction Thrust Faults, MARGINS Theoretical and Experimental Earth Science Series, Columbia Univ press, New York, USA, pp 545–575

Wang CS, Liou YA, Yeh TK (2008) Impact of surface meteorological measurements on GPS height determination. Geophys Res Lett 35:L23809. doi:10.1029/2008GL035929

Wernicke B, Davis JL, Bennett RA, Normandeau JE, Friedrich AM (2004) Tectonic implications of a dense continuous GPS velocity field at Yucca Mountain, Nevada. J Geophys Res 109:B12404

Wyss M, Slater L, Burford RO (1990) Decrease in deformation rate as a possible precursor to the next Parkfield earthquake. Nature 345:428–431. doi:10.1038/345428a0

Xu G (2007) GPS–Theory, Algorithms and Applications, 2nd edn. Springer, Heidelberg

Yeh TK, Hwang C, Xu G (2008) GPS height and gravity variations due to ocean tidal loading around Taiwan. Surv Geophys 29:37–50

Yeh TK, Hwang C, Xu G, Wang CS, Lee CC (2009) Determination of global positioning system (GPS) receiver clock errors: impact on positioning accuracy. Meas Sci Technol 20:075105. doi:10.1088/0957-0233/20/7/075105

Yen YT, Ma KF, Wen YY (2008) Slip partition of the 26 December 2006 Pingtung, Taiwan (M 6.9, M 6.8) earthquake doublet determined from teleseismic waveforms. Terr Atmos Ocean Sci 19:567–578. doi:10.3319/TAO.2008.19.6.567

Yu SB, Chen HY, Kuo LC (1997) Velocity field of GPS stations in the Taiwan area. Tectonophysics 274:41–59

Yu SB, Kuo LC, Hsu YJ, Su HH, Liu CC, Hou CS, Lee JF, Lai TC, Liu CC, Liu CL, Tseng TF, Tsai CS, Shin TC (2001) Preseismic deformation and coseismic displacements associated with the 1999 Chi-Chi, Taiwan earthquake. Bull Seism Soc Am 91:995–1012

Yu SB, Hsu YJ, Kuo LC, Chen HY, Liu CC (2003) GPS measurement of postseismic deformation following the 1999 Chi-Chi, Taiwan earthquake. J Geophys Res 108:2520. doi:10.1029/2003JB002396